



# Hierarchical zeolitic imidazolate framework-derived manganese-doped zinc oxide decorated carbon nanofiber electrodes for high performance flexible supercapacitors

Edmund Samuel<sup>a,1</sup>, Bhavana Joshi<sup>a,1</sup>, Min-Woo Kim<sup>a</sup>, Yong-Il Kim<sup>a</sup>, Mark T. Swihart<sup>b</sup>, Sam S. Yoon<sup>a,\*</sup>

<sup>a</sup> School of Mechanical Engineering, Korea University, Seoul 136-713, Republic of Korea

<sup>b</sup> Department of Chemical & Biological Engineering and RENEW Institute, University at Buffalo, The State University of New York, Buffalo, NY 14260-4200, USA

## HIGHLIGHTS

- Electrospun nanofiber mats are surface-decorated with Mn-doped ZIF-8 nanoparticles.
- Freestanding flexible Mn@ZnO/CNF is demonstrated as a promising supercapacitor electrode.
- Enhanced capacitance of 501 F·g<sup>-1</sup> and 92% capacitance retention after 10,000 cycles are obtained.

## ARTICLE INFO

### Keywords:

Mn/ZIF-8  
Carbon nanofiber  
Supercapacitor  
Electrospinning

## ABSTRACT

We demonstrate freestanding, flexible, and cost-effective supercapacitor electrodes comprising carbon nanofibers (CNFs) decorated with metal oxide framework (MOF)-derived manganese-doped zinc oxide (Mn@ZnO). Nanoparticles of manganese-doped zeolitic imidazolate framework (ZIF-8) were grown directly on electrospun polyacrylonitrile nanofibers by a simple solution-phase synthesis. Carbonization of these composite fibers produced high surface area dodecahedral Mn@ZnO on core CNFs that provide fast electron-transfer pathways. The synergy between Mn@ZnO (active sites for Faradaic reactions) and the highly electrically conductive carbon nanofiber improves the performance of the supercapacitor electrode. The Mn@ZnO/CNF electrodes exhibit a high specific capacitance of 501 F·g<sup>-1</sup> and retain > 92% of their initial capacitance after 10,000 cycles. The optimized Mn@ZnO/CNF electrodes deliver impressive energy densities of 72.1 W·h·kg<sup>-1</sup> and 33.3 W·h·kg<sup>-1</sup> at power densities of 500 W·kg<sup>-1</sup> and 5000 W·kg<sup>-1</sup>, respectively. This electrochemical performance demonstrates that the Mn@ZnO/CNF nanostructured composite is a robust electrode material for long-lifetime high-rate energy storage/delivery devices.

## 1. Introduction

Demand for portable energy storage devices to power systems ranging from flexible electronics to electrical vehicles is rapidly increasing [1,2]. These applications require both fast charging and high energy density [3,4]. Supercapacitors (SCs) can be rapidly charged/discharged, and can therefore play an important role, alone or in combination with batteries, in these applications. The three major phenomena associated with SCs are electrochemical double-layer capacitance (EDLC), pseudocapacitance, and corrosion/decomposition of electrodes or electrolyte [5–7]. The first two phenomena are essential for high-stability and

high-energy-density SCs. In general, EDLC occurs in high surface area carbon materials by accumulating charges at their surfaces. The maximum concentration of ions that can accumulate per surface area limits EDLC to relatively low energy density [8]. Some metal oxides, particularly RuO<sub>2</sub> [9] and MnO<sub>2</sub> [10,11] exhibit the electrochemical signature of capacitive electrodes (pseudocapacitance) via a fast interfacial electron-transfer mechanism rather than simple ion adsorption [12], thereby providing higher energy densities. However, electrode corrosion and electrolyte decomposition in such systems can lead to degradation and drastic capacitance loss within a few thousand cycles [13,14]. Achieving high capacity and long-term stability using

\* Corresponding author.

E-mail address: [skymoon@korea.ac.kr](mailto:skymoon@korea.ac.kr) (S.S. Yoon).

<sup>1</sup> These authors have contributed equally.

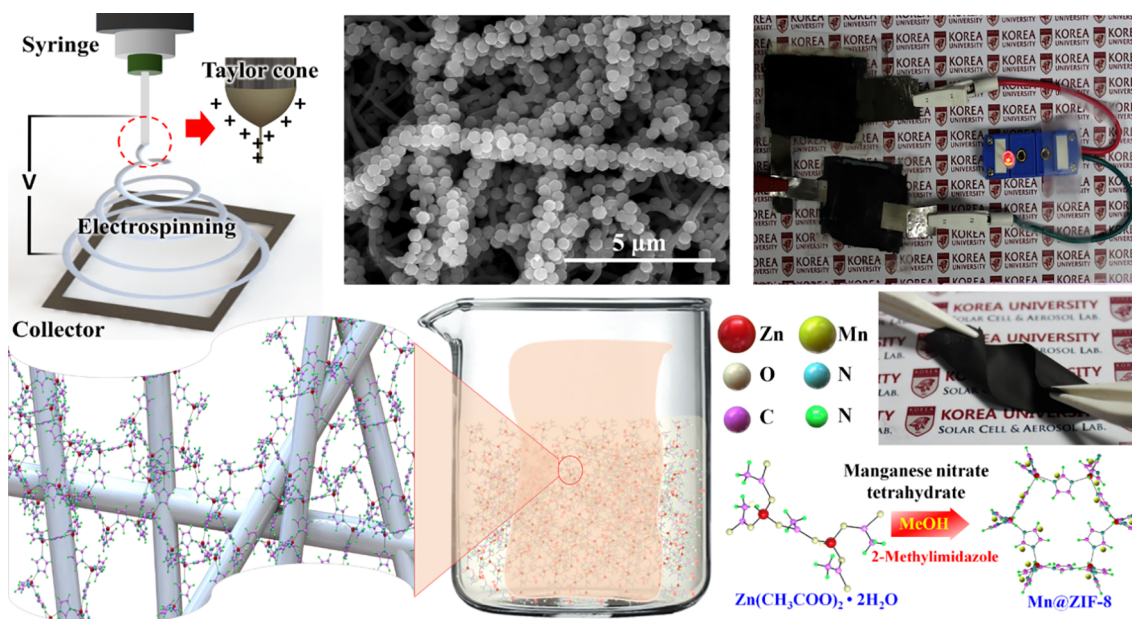


**Fig. 1.** Schematic of the fabrication of freestanding and flexible Mn@ZnO/CNFs. Upper row: Electrospinning setup, SEM image showing the morphology of Mn@ZnO/CNF, and photograph of flexible electrodes powering an LED. Lower row: Diagram showing loading of Mn@ZIF-8 over NFs in a beaker during reaction, atomic structures of reactants for producing Mn@ZIF-8, and a photograph showing the flexibility of an electrode sample.

combinations of carbon, metal oxides, and electrolytes remains challenging. Composite active materials for SC electrodes, using carbon and multiple metal oxides, have emerged as a promising approach to simultaneously achieve high energy density and good stability [15].

In recent years, metal-organic framework (MOF)-derived materials have attracted much attention in supercapacitor research because of their potential to provide high energy storage rates and densities [16]. MOFs, which are synthesized from metal ions and organic ligands, have metal-ligand coordination structures that produce porous, ultrahigh-surface area structures [17]. Carbonization of a MOF by heat treatment (high temperature pyrolysis) can maintain this high surface area structure to provide well-dispersed metal oxide sites on a high surface area porous carbon framework. Because energy storage (via both EDLC and pseudocapacitive Faradaic reactions) occurs at the SC electrode/electrolyte interface, the addition of pseudocapacitive metal oxides on these high surface area materials increases the rate and capacity for charge storage [18]. Under the appropriate pyrolysis conditions, MOFs retain their porous morphologies and ion diffusion pathways within their host architectures [19,20]. Numerous MOFs have been investigated for energy harvesting and storage in fuel cells [21], lithium-ion batteries [22–24], and SCs [25], where this high porosity and large surface area are advantageous [26].

Zeolitic imidazolate framework (ZIF-8)-derived composites as flexible electrodes for SCs have not yet been extensively explored. ZIF-8, featuring tetrahedrally coordinated  $Zn^{2+}$  linked with N atoms of imidazolate, has an architecture that could provide excellent ion sorption and storage, particularly if pseudocapacitive metal oxides are incorporated into it. However, reports on ZIF-8-derived materials containing multiple metal ions for SC applications are scarce [27–32]. Kadota et al. reported formation of distorted crystal structures of Mn@ZIF-8 via a solvothermal reaction using Mn-acetate and Mn-nitrate, where  $Mn^{2+}$  replaced  $Zn^{2+}$ . To maintain the geometric coordination of ZIF-8,  $Mn^{2+}$  should theoretically sustain the topology [33]. Synthesis of cobalt and zinc decorated ZIF has been explored; however, manganese-decorated ZIF-derived materials have not yet been studied for supercapacitor applications, despite their potential high performance [28]. In general, manganese-based composite materials are promising for SC electrodes because of their excellent pseudocapacitance characteristics, wide potential range, low cost, and environmental friendliness [10].

Further, the presence of heteroatoms such as nitrogen in ZIF-8 can change the electron transfer characteristics of the carbon composites and promote interfacial capacitance by the pseudocapacitive effect.

Hence, in this study, we fabricate and test the electrochemical performance of CNFs decorated with Mn@ZnO (Mn-doped porous dodecahedral or star-shaped ZnO derived from ZIF-8). To the best of our knowledge, such Mn@ZIF-8/CNF composites have not been studied for SC applications. The Mn@ZnO/CNF freestanding SC electrode shows significantly improved ion adsorption and charge-transfer because Mn metal centers decorate ZnO, stabilize the metal oxide, and provide pseudocapacitance. These freestanding SC electrodes show excellent stable electrochemical performance at high current densities and after long-term cycling.

## 2. Experimental procedures

### 2.1. Electrospinning of nanofiber

Precursors for nanocomposite electrode fabrication included zinc acetate dihydrate ( $ZnAc$ ,  $Zn(CH_3COO)_2 \cdot 2H_2O$ , Oriental Chemical Industries, South Korea), manganese nitrate tetrahydrate (Mn-nitrate,  $Mn(NO_3)_2 \cdot 4H_2O$ , Sigma-Aldrich, USA), 2-methylimidazole (2MI,  $C_4H_6N_2$ , Sigma-Aldrich, USA), and polyacrylonitrile (PAN,  $M_w = 150$  kDa, Sigma-Aldrich, USA). *N,N*-dimethylformamide (DMF, 99.8%, Sigma-Aldrich, USA), and methanol (MeOH,  $CH_3OH$ , Duksan Chemicals, South Korea) were used as solvents. To form the nanofiber (NF) precursor solution, 0.8 g of PAN and 0.08 g of 2MI were mixed with DMF for 24 h. 2MI was used in the fiber synthesis to seed growth of ZIF-8 on the fiber in the subsequent step. The fully-mixed PAN/2MI solution was electrospun onto a drum collector to obtain a PAN-2MI textile for further processing. For electrospinning, the solution was placed in a syringe (as shown in Fig. 1) connected to a 0.84-mm-diameter needle. To maintain the cone-jet and to produce uniform CNFs, the flow rate of the solution was optimized to 250  $\mu$ L/h. The voltage applied between the needle and drum collector, placed 13 cm away, was 7 kV. The as-deposited PAN-2MI NF formed a textile of 30  $\times$  10  $cm^2$ .

## 2.2. Loading of Mn@ZIF-8/CNF

The approach for NF production and Mn@ZIF-8 decoration of the NFs is illustrated schematically in Fig. 1. Mn-ZIF-8 solutions were prepared containing 2, 5, or 7 mM Mn-nitrate and 10 mM ZnAc in 50 mL MeOH. Once the salts were completely dissolved, 40 mM concentration of 2MI was added, and the solution was stirred for 10 min to induce precipitation, which indicated the beginning of ZIF-8 formation. The as-deposited PAN-2MI NF textile was masked in a polyethylene terephthalate (PET) frame to hold the fibers flat without any wrinkles due to curling/twisting in the ZIF-8 solution. These PET-masked PAN-2MI fibers were soaked in the precursor solution for 110 min, yielding Mn-ZIF-8-decorated NFs. The NFs were then washed with clean MeOH and dried for 24 h at room temperature of  $\sim 25^\circ\text{C}$ . These dried fibers were then stabilized by heating for 30 min at  $150^\circ\text{C}$  with a ramp rate of  $5^\circ\text{C}/\text{min}$ . The stabilized fibers were then carbonized in Ar at  $800^\circ\text{C}$  for 1 h with a ramp rate of  $3^\circ\text{C}/\text{min}$ . The obtained fibers were black in color and freestanding. We refer to the samples prepared using 2, 5, and 7 mM Mn as M1, M2, and M3, respectively. For comparison, pure CNF and ZnO/CNF (without Mn) were also tested. We refer to these samples as CNF and M0, respectively.

## 2.3. Physicochemical characterization

X-ray diffraction (XRD; SmartLab, Rigaku) was employed to probe the crystalline phases present in the composites. A Raman spectrometer (NRS-3100, Jasco) was used to analyze their graphitic and disordered carbon content. The morphologies of the Mn@ZnO/CNFs were observed using a field-emission scanning electron microscope (FESEM; S-5000, Hitachi, Ltd.) and a transmission electron microscope (TEM; JEM 2100F, JEOL Inc.). The TEM samples were prepared by dropping a thin loaded fiber sample onto a Cu grid 12 h before characterization. Energy-dispersive X-ray (EDX) spectrometers configured within the SEM and TEM were used for elemental mapping at low and high resolution, respectively. X-ray photoelectron spectroscopy (XPS; Theta Probe Base System, Thermo Fisher Scientific Co.) was used to probe elemental compositions and chemical states.

## 2.4. Electrochemical characterization

The annealed samples were binder-free, freestanding, and flexible enough to be punched into 14-mm circular mats and assembled as symmetric SCs in CR2032 coin-type cells. A Celgard 3501 (Celgard, Chungbuk, South Korea) polymer membrane was used for electrical isolation of the two electrodes; 6-M KOH served as the aqueous electrolyte. The cells were subjected to electrochemical impedance spectroscopy (EIS) measurement (VersaSTAT-3, Princeton Applied Research, USA) over a frequency range of 100 kHz–0.1 Hz. After EIS, cyclic voltammetry (CV) and galvanostatic charge–discharge (GCD) tests were performed over a voltage range of 0–1 V at  $25^\circ\text{C}$  using a WBCS3000 battery cycler system (WonA Tech, South Korea). The SC cells were tested at various scan rates and current densities for CV and GCD cycling, respectively.

## 3. Results and discussion

### 3.1. Material properties

Carbonization of the Mn-ZIF-8-decorated fibers under Ar transforms them into Mn@ZnO/CNF; their XRD patterns in Fig. 2a show crystallographic peaks at  $28^\circ$  (JCPDS No. 21-1486),  $47^\circ$ , and  $56^\circ$  (JCPDS No. 36-1451), indicating the formation of ZnO [34]. However, the carbonization in Ar impedes the oxidation and further crystallization of Mn/ZnO; hence, no MnO peaks are observed. Furthermore, the C is mainly in amorphous form, as demonstrated by the very broad peak at  $\sim 22^\circ$ . Before carbonization, Mn@ZIF-8 formation was characterized by

comparing the diffraction peaks of the sample (see Fig. S1) with simulated patterns of ZIF-8 from the literature [35,36], which confirmed the ZIF-8 Zn–N sodalite topology. The addition of Mn changed the intensities of some XRD peaks, but did not inhibit the formation of ZIF-8. The XRD pattern of sample M0 presented in Fig. S2 is similar to other carbonized samples showing peaks from ZnO.

The Raman spectra of the composites (Fig. 2b) show bands centered at  $1355\text{ cm}^{-1}$  and  $1585\text{ cm}^{-1}$ , which are attributed to defective (D) and graphitic (G) carbon, respectively [37]. The relative intensity ratio of the D to G bands ( $I_D/I_G$ ) indicates the degree of graphitization. This ratio remained the same,  $\sim 1.5$ , for all of the carbonized Mn@ZnO/CNF samples, suggesting that the samples contain defective carbon that provides more reactive sites for electrochemical reactions than highly graphitic carbon.

SEM images of samples M1, M2, and M3 with different Mn concentrations are presented in Fig. 3 at various magnifications. The SEM of the pristine CNF and M0 samples are shown in Fig. S3 at various magnifications. The surfaces of the CNFs are decorated with characteristic rhombic dodecahedral particles derived from ZIF-8. At low Mn concentration (sample M1) the morphology is uniform and typical of ZIF-8-derived material, while the particles become slightly smaller and less uniform with increasing Mn addition [38,39]. The reduced dodecahedral particle size of M1 and M2 compared to that of M0 (Figs. 3 and S3) is attributed to the presence of Mn ions that increase nucleation density via direct reaction of Mn ions (replacing Zn ions) and organic ligand (2MI). However, further increasing the concentration of Mn (M3) may lead to structural instability of  $\text{Mn}^{2+}$ –4N. This limits exchange of the Zn–Mn ions and thus the morphology is significantly modified. Additionally, in the M3 case, the size increases as excess Mn (7 mM Mn concentration) cannot fully incorporate into the dodecahedral structure and Mn ions may be concentrated at the surface of the Mn/ZIF-8 structures [38,40]. Thus, with further addition of Mn, the concave truncation is more distinct in the M2 and M3 sample images. Higher-resolution SEM images of M1, M2 and M3 samples are presented in Fig. S5. Elemental mapping data for the M1, M2, and M3 samples are presented in the supporting information (Fig. S5); elemental compositions are provided in Table S1. The EDS spectra for all three samples are shown in Fig. S6.

TEM images of M2 exhibit star-like structures (Fig. 4a, b) connected to NFs, confirming particle loading on the CNFs. The high-resolution TEM (HRTEM) image in Fig. 4c does not show clear lattice fringes, but the selected-area electron diffraction (SAED) pattern in the inset of Fig. 4c shows diffuse rings attributed to the (1 0 1) and (1 0 2) planes of ZnO. The HRTEM image also clearly illustrates the rhombic dodecahedral morphology derived from ZIF-8. The star shape is distinctly visible in the elemental maps shown in Fig. 4d, whereas empty areas at the corners of the star show the natural porous structure inherited from the parent ZIF-8. The presence of Zn, C, Mn, and O confirms the uniform distribution of elements in the ZIF-8-derived ZnO, with Mn alongside Zn. Thus, the SEM and TEM images demonstrate that the obtained Mn@ZnO retains the ZIF-8 morphology after carbonization.

XPS was used to determine the chemical states of the elements. The survey spectrum (Fig. 5a) confirms the presence of C, N, O, Zn, and Mn in sample M2. Fig. 5b shows a high-resolution spectrum of Zn 2p that clearly shows peaks at 1021.4 and 1044.8 eV. The spin-orbit splitting of Zn 2p is 23.4 eV, consistent with the  $\text{Zn}^{2+}$  state. Shoulder peaks are also observed at 1022 and 1045.6 eV with a binding energy difference of 24 eV, also corresponding to ZnO. The high-resolution O 1s spectrum (Fig. 5c) can be deconvoluted into three peaks; the peak at 531 eV belongs to metal oxide (Zn–O), whereas those at 523.2 and 533 eV are attributed to Zn–O–H and –OH from adsorbed moisture, respectively. The Mn 2p spectrum in (Fig. 5d) shows two characteristic peak positions of Mn 2p<sub>3/2</sub> and Mn 2p<sub>1/2</sub> with a binding energy difference of  $\sim 12.3$  eV. The observed binding energy peaks are broad and asymmetric, indicating the coexistence of Mn in multiple oxidation states as  $\text{Mn}^{2+}$ ,  $\text{Mn}^{3+}$ , and  $\text{Mn}^{4+}$  [41–44]. The peak at a lower binding energy

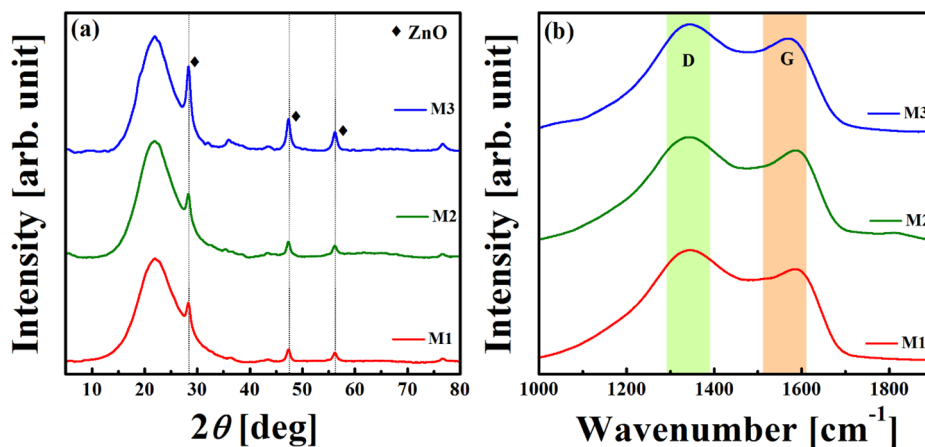


Fig. 2. (a) XRD patterns and (b) Raman spectra of M1, M2, and M3.

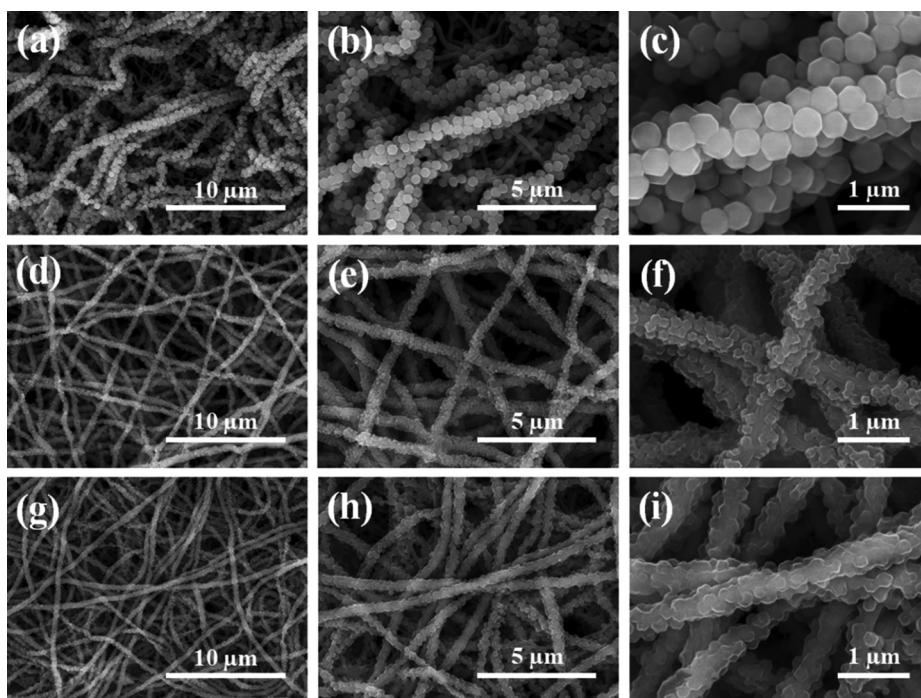


Fig. 3. SEM images of the Mn@ZnO-decorated CNF samples: M1 (a-c), M2 (d-f), and M3 (g-i).

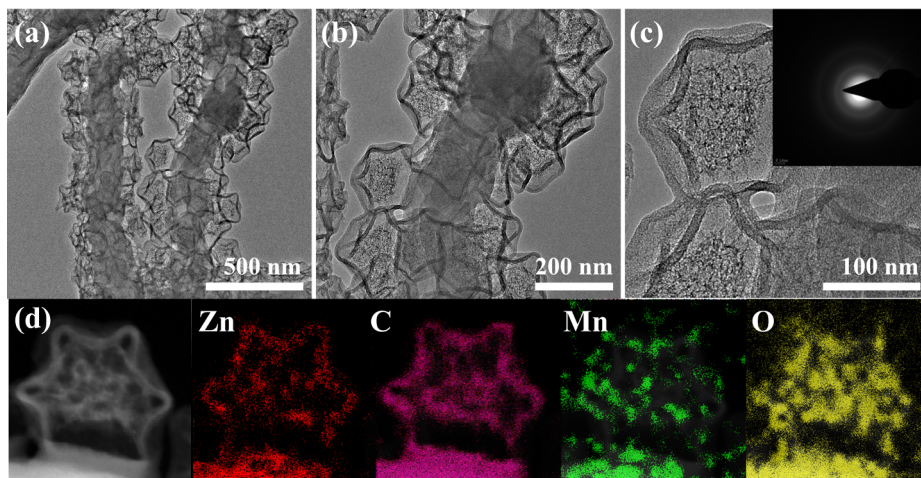


Fig. 4. (a), (b) TEM images, (c) high-resolution TEM (HRTEM) image and (d) EDS-based elemental maps of Zn, C, Mn, and O in carbonized Mn@ZnO/CNF composite (M2). The inset of (c) shows the corresponding selected-area electron diffraction (SAED) pattern.

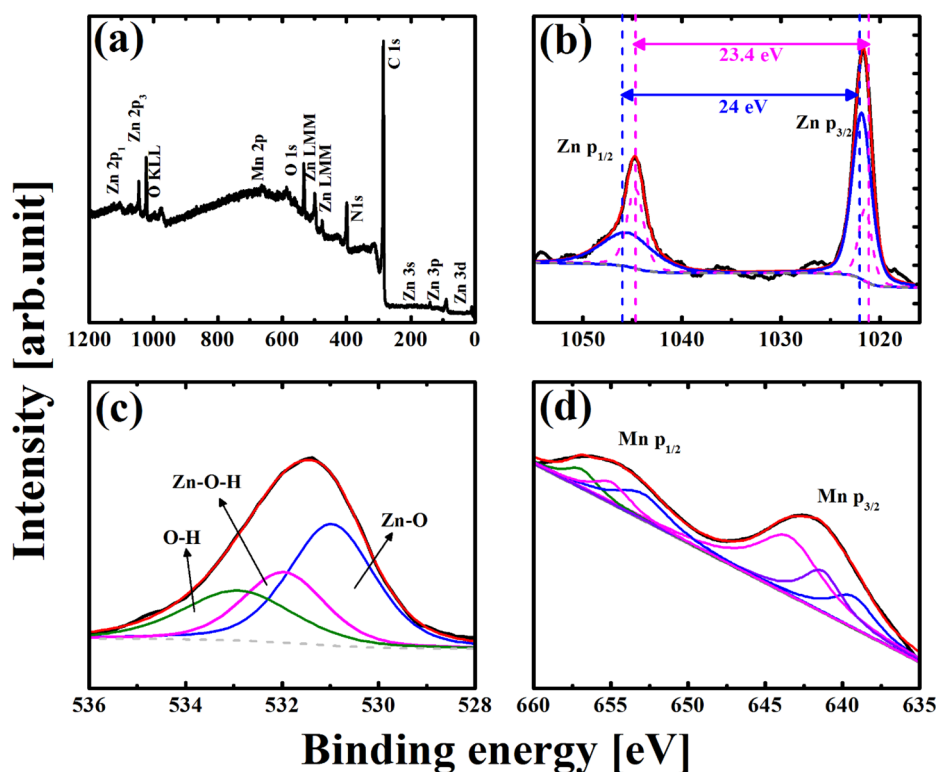


Fig. 5. (a) Survey XPS spectrum and core XPS spectra of (b) Zn, (c) O, and (d) Mn for sample M2.

of 639 eV suggest the existence of metallic Mn [10,33]. The chemical environment of nitrogen in the sample was also analyzed by XPS N1s spectra as shown in Fig. S7. Pyridinic, pyrolic, graphitic, and oxidized nitrogen are present, as demonstrated by the peaks at 397.3, 398, 399 and 400.3 eV, respectively. The spectrum shows the presence of the pyridinic and graphitic structures incorporated in the composite samples. The pyridinic nitrogen is present in the defective sites of carbon whereas the graphitic nitrogen substitutes for carbon in the graphene framework. The pyridinic and graphitic nitrogen enhance electrical conductivity due to the difference in electronegativity of N and C.

### 3.2. Electrochemical performance

The CNF decorated with dodecahedral ZnO provided additional electrochemical sites and enhanced energy storage capability. The improved electrochemical response is demonstrated by the broader CV curve of ZnO@CNF (M0) compared to that of CNF, as shown in Fig. S8a. CV curves for the Mn-doped ZnO@CNF (M1, M2, and M3) samples are shown in Fig. 6a-c, over a range of scan rates, using an aqueous electrolyte (6-M KOH) and potential window range of 0–1 V. The Mn-doped samples exhibit increased pseudocapacitive characteristics, increasing their energy storage capacity. The CV curves clearly suggest that the electrochemical performance of M2 is superior to that of M1 and M3. Although M3 exhibits the highest limiting current, the superiority of M2 is inferred from its larger integrated curve area (larger average current over the scan). The electrochemical performance of sample M2 (see Fig. S8a) improves because of the optimal Mn doping and increased density of electrochemically active sites. In Fig. 6c, a slight deviation in the linearity of the CV curve for M3 indicates complex kinetics of electron transfer, possibly from increased resistive characteristics. This deviation may be due to reduced interaction space. The anodic and cathodic peak currents of sample M3 are higher than those of M2. In the case of M1, the lower amount of Mn allows formation of characteristic ZIF-8 structures and thus the EDLC behavior dominates. Sample M2 still retains characteristic ZIF-8 structure and comparatively smaller

dodecahedral particle size, but the presence of  $\text{Mn}^{2+} - 4\text{N}$  results in the exchange of Zn and Mn ions at the ligand sites [40]. The presence more Mn in the framework and smaller particle size produces a synergetic combination of EDLC and pseudocapacitive performance compared to that of samples M1 and M3. However, the resistive-capacitor characteristics of M3 are more dominant, as indicated by the smaller integrated area under the CV curve, as shown in Fig. S8b.

As the Mn concentration increases, the dodecahedral three-dimensional framework merges. Also, from the SEM images (see Fig. 3), the Mn@ZnO/C particles derived from ZIF-8 are distorted. The M3 samples suffer from the diffusion limitations and interphase resistance to the electrolyte [45]. Additionally, active material resistance at the surface appears as the organic framework is covered by a layer of Mn. The narrow and inclined cyclic voltammograms clearly display the limitation of the Mn-rich sample (M3) in Fig. 6c. However, narrower CV curves of sample M3 suggest a sharp drop of EDL capacitance due to limited diffusion of the electrolyte ions.

The recorded CV curves at different scan rates were used to establish the electrochemical redox system. The peak anodic/cathodic currents exhibit linear dependence on the square root of the scan rate, as shown in Fig. 6d, consistent with reversible electron transfer in the SC cell. The anodic/cathodic peak currents at  $100 \text{ mV}\cdot\text{s}^{-1}$  for M1, M2, and M3 were compared to those of CNF and M0 in Fig. S8c. The low peak current response of CNF is because only EDLC occurs, while in other samples EDLC and redox reactions occur simultaneously, as shown schematically in Fig. S8d. This also confirms that Mn doping is effective for increasing energy storage capacity. Fig. 6e and f demonstrates the flexibility of the fabricated supercapacitor bent at different angles. The CV curves (at a scan rate of  $100 \text{ mV}\cdot\text{s}^{-1}$ ) in Fig. 6e show that the supercapacitor is unaffected by bending.

The galvanostatic technique, which controls the current and measures the corresponding voltage, is the standard approach for measuring the specific capacitance of electrodes. The specific capacitance  $C_s$  is deduced using the following relation:

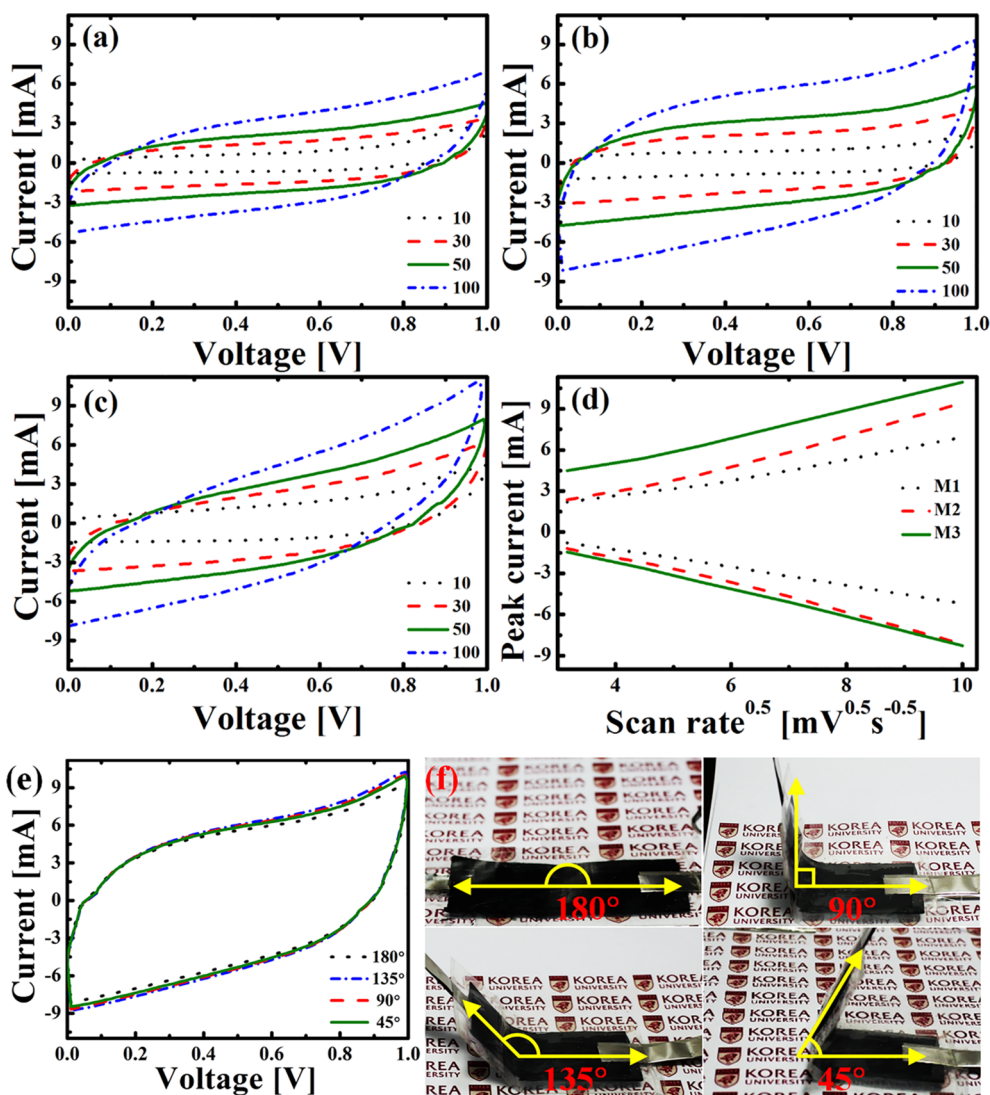


**Fig. 6.** CV for samples (a) M1, (b) M2, and (c) M3 at different scan rates ( $\text{mV s}^{-1}$ ) as labelled; (d) peak current vs. square root of the scan rate, derived from CV curves for the same samples, at different scan rates. (e) CV curves of the flexible symmetric SC bent at different angles ( $180^\circ$ ,  $135^\circ$ ,  $90^\circ$  and  $45^\circ$ ) at a scan rate of  $100 \text{ mV/s}$ . (f) Photographs of the flexible symmetric SC bent at different angles.

$$C_s = \frac{4I}{m \times \Delta V / \Delta t} \quad (1)$$

where  $I$  is the applied constant current,  $\Delta t$  the discharge time,  $m$  the total mass of the two electrodes, and  $\Delta V$  the potential window of charging/discharging [46].

The capacitive responses of the Mn@ZnO/CNF materials were assessed by GCD measurements. Fig. 7a-c shows the galvanostatic charge/discharge curves for current densities of  $1\text{--}10 \text{ A g}^{-1}$  for different samples. The charge/discharge curves show linear responses for each symmetric SC cell, suggesting good supercapacitive characteristics. As shown in Fig. 7a-c, sample M2 demonstrates the longest charging and discharging curves at fixed current density, compared to samples M1 and M3. As the current density increases, electrolyte ions cannot reach all available active sites of the electrodes, and the capacitance decreases. The specific capacitances are deduced from the discharge times at different current densities for all cases.

Fig. 7d shows the capacitances of  $394$ ,  $501$ , and  $438 \text{ F g}^{-1}$  at a current density of  $1 \text{ A g}^{-1}$  for samples M1, M2, and M3, respectively. As the current density is increased to  $10 \text{ A g}^{-1}$ , the capacitances decrease to  $170$ ,  $230$ , and  $190 \text{ F g}^{-1}$ , respectively. The capacitances of M1 and M3 are significantly lower than that of M2; the decrease in specific capacitance with increasing current density is similar for all cases,

reaching  $57\%$  for M1 and M3 and  $54\%$  for M2; (see Table S2). Table 1 compares the specific capacitances attained in previous studies that used ZIF-8 based materials for SC electrodes. The lack of sudden voltage drops due to internal resistance (IR), which indicates reversible redox reaction capabilities of the samples, is notable. Additionally, the high pseudocapacitance and linear discharge curves can be attributed to the three-dimensional porous Mn@ZnO frameworks decorated on the CNFs. Here, the Mn@ZnO polyhedral structure is effectively used to store energy and CNFs are employed for efficient electron transfer.

The most important advantage of a SC in applications is its fast delivery of very high currents compared to other energy storage devices, such as batteries. Fig. 8a presents a Ragone plot demonstrating the specific energies and power densities of the Mn@ZnO dodecahedron-decorated CNF samples. M2 delivers an excellent energy density of  $72.1 \text{ Wh kg}^{-1}$  at  $500 \text{ W kg}^{-1}$  and retains  $33.3 \text{ Wh kg}^{-1}$  at a high power density of  $5000 \text{ W kg}^{-1}$ . The energy densities are calculated using the specific capacitances presented in Fig. 7d; the relation of specific capacitance and energy density is  $E = \frac{C_s V^2}{2}$ . The energy densities exhibited by M2 at low and high power densities are far better than those of other reported materials, as compared in Fig. 8b and Table 1, and are also much better than those of samples M1 and M3, as shown in Fig. 8a and b. The high energy density is attributed to the porous dodecahedron-

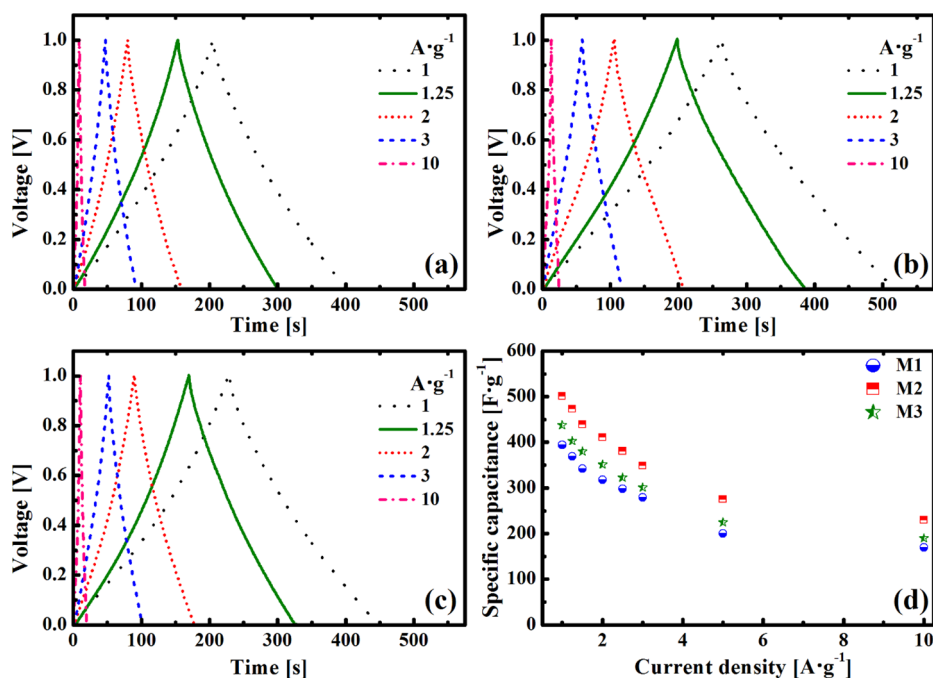


Fig. 7. GCD profiles of Mn@ZnO/CNF (a) M1, (b) M2, and (c) M3 at various current densities. (d) The specific capacitances of M1, M2, and M3 vs. current density.

Table 1

Comparison of electrochemical performance of our electrode with those in previously reported studies.

Materials	Capacitance [F·g <sup>-1</sup> ]	Current density [A·g <sup>-1</sup> ]	Potential window [V]	Electrolyte	Ref.
ZIF-8/MWCNT	113	0.5	0–0.9	1 M H <sub>2</sub> SO <sub>4</sub>	[48]
ZIF-8 derived carbon	250	1	–0.3 to 0.7	1 M Na <sub>2</sub> SO <sub>4</sub>	[49]
ZIF-8 derived 3D hybrid porous carbon	332	0.5	0–1	6 M KOH	[50]
ZIF-8	98	0.5	0–0.9	1 M H <sub>2</sub> SO <sub>4</sub>	[51]
ZIF-8 derived Carbon	56.6	0.1	0–0.8	1 M H <sub>2</sub> SO <sub>4</sub>	[52]
ZIF-8/MWCNT	326	1	0–1	1 M H <sub>2</sub> SO <sub>4</sub>	[53]
ZIF-8 derived Broccoli-like porous carbon	359	1	–1 to 0	6 M KOH	[43]
ZIF-8/graphene	245	1	–1 to 0	6 M KOH	[54]
ZIF-8 derived carbon /g-CN	495	0.1	0–0.8	1 M H <sub>2</sub> SO <sub>4</sub>	[55]
ZIF-8 derived N-doped PC	245	1	–1 to 0	6 M KOH	[56]
Mn@ZIF-8	501	1	0–1	6 M KOH	Present

decorated carbon matrix, as Mn@ZnO provides enhanced energy-storage active sites and carbon offers fast charge-transport pathways. Additionally, the uniform loading of Mn@ZnO over the CNF (see Figs. 3 and S5) ensures that enhanced energy storage sites are available at the electrode/electrolyte interfaces.

The long-term cycling performance of symmetric SCs is essential for advanced applications. To assess long-term performance, the symmetric SC cells were cycled over the potential window of 0–1 V for 10,000 continuous GCD cycles at current densities of 1.0 and 5 A·g<sup>-1</sup>. The excellent capacitance retention of sample M2 as a function of galvanostatic cycle number is shown in Fig. 8c. The capacitance retention of Mn@ZnO/CNF (~92% and 84% at current densities of 1 A·g<sup>-1</sup> and 5 A·g<sup>-1</sup>) is superior to many previously reported ZIF-8 based electrodes. The capacitance retention and number of GCD cycles for some of the ZIF-8 based metal/bimetallic oxide are, SnO<sub>2</sub>@ZIF-8 (72% after 500 cycles) [27], ZIF-8@cetyltrimethylammonium bromide (92% after 1000 cycles) [47], multi-walled carbon nanotube (CNT)@ZIF-8 (95.8% after 10,000 cycles) [48], ZIF-8-derived nanoporous carbon/CNT (93.5% after 1000 cycles) [30], ZIF-8@C/NiAl (77% after 1000 cycles) [31], and MnO<sub>2</sub>/ZIF-8-derived carbon (57% after 1000 cycles) [32]. The high capacitance retention arises from the well-dispersed Mn, Zn, and carbon (see Fig. S3), which provide better interlinking of chemically bonded components and faster electron-transfer pathways, thereby achieving stable electrochemical performance.

EIS allows us to analyze the charge-transfer capability between the electrochemical sites of the active materials of the SC electrode. The plot of imaginary impedance ( $Z_{im}$ ) as a function of the real impedance ( $Z_{re}$ ) is known as a Nyquist plot. Fig. 8d shows Nyquist plots for samples M1, M2, and M3. The data for each sample was fit to Randle's equivalent circuit, as shown in Fig. S9. The basic elements shown in Fig. S9 are the solution resistance ( $R_s$ ), charge-transfer resistance ( $R_{ct}$ ), depletion-layer resistance ( $R_{dl}$ ), capacitance (C), and the constant-phase element (CPE or Q). The physicochemical response to charge-transfer activation between the electrode and electrolyte is indicated by  $R_s$ , ohmic losses by  $R_{ct}$ , double-layer capacitance by C, and microscopic material properties by CPE (see Fig. S9). The resistances  $R_s$  (11.8, 8.3, and 7.1  $\Omega$ ) and  $R_{ct}$  (213.3, 99.8, and 60.4  $\Omega$ ) decrease with increasing Mn content for samples M1, M2, and M3, respectively. All samples show semicircles, indicating good capacitive characteristics, and linear Warburg regions indicating ionic diffusion in the available pores and internal surfaces of the dodecahedra and CNF.

#### 4. Conclusions

In summary, we demonstrated decoration of CNFs with bimetallic ZIF-8 derived Mn@ZnO dodecahedral nanoparticles via a facile synthesis approach and optimized the Mn concentration to provide superior electrochemical performance and stability as a SC electrode material.

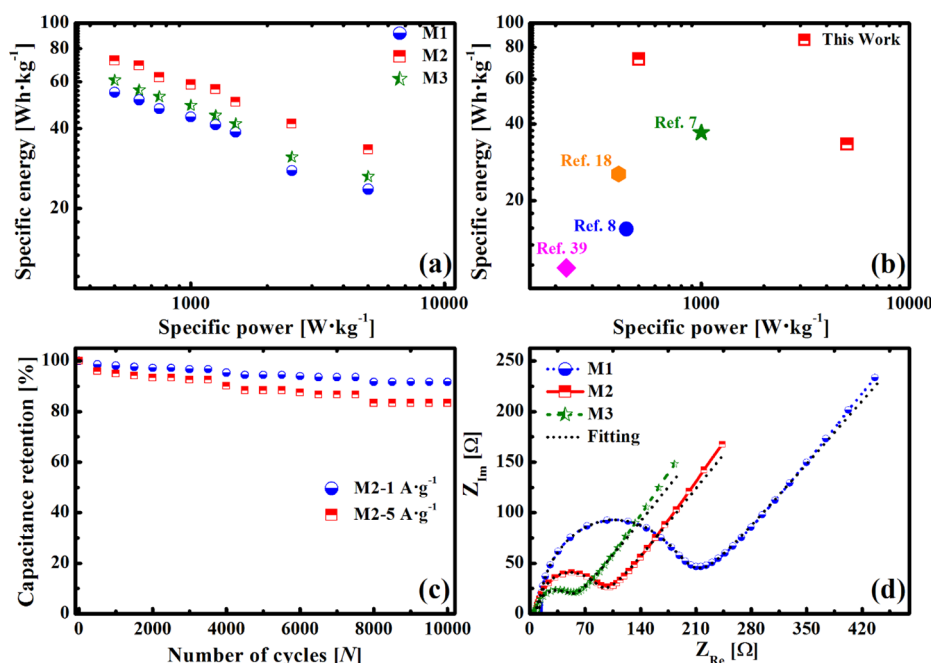


**Fig. 8.** (a) Ragone plots for samples M1, M2, and M3, (b) comparison of energy and power densities with previous reports, (c) capacitance retention under long-term galvanostatic cycling at low and high current densities for sample M2, and (d) Nyquist plots of EIS data.

The electrochemical responses at different scan rates and specific currents suggest that the M2 sample, fabricated with 5 mM Mn concentration, provides optimal synergy for excellent capacitance retention after 10,000 GCD cycles. The optimized Mn@ZnO/CNF electrodes deliver impressive energy densities of 72.1 Wh·kg<sup>-1</sup> and 33.3 Wh·kg<sup>-1</sup> at power densities of 500 W·kg<sup>-1</sup> and 5000 W·kg<sup>-1</sup>, respectively. The facile synthesis process for producing a carbon-mixed metal oxide three-dimensional morphology provides a significant opportunity for the development of scalable freestanding SC electrodes for rapid energy storage.

## Acknowledgements

This research was supported by the Technology Development Program to Solve Climate Changes of the National Research Foundation (NRF) funded by the Ministry of Science, ICT & Future Planning (NRF-2016M1A2A2936760), NRF-2013R1A5A1073861, and NRF-2017R1A2B4005639.

## Appendix A. Supplementary data

Supplementary data to this article can be found online at <https://doi.org/10.1016/j.cej.2019.04.065>.

## References

- [1] S. Yong, J. Owen, S. Beeby, Solid-state supercapacitor fabricated in a single woven textile layer for E-textiles applications, *Adv. Eng. Mater.* 20 (2018) 1700860.
- [2] E. Samuel, B. Joshi, H.S. Jo, Y.I. Kim, M.T. Swihart, J.M. Yun, K.H. Kim, S.S. Yoon, Flexible and freestanding core-shell SnO<sub>x</sub>/carbon nanofiber mats for high-performance supercapacitors, *J. Alloy. Compd.* 728 (2017) 1362–1371.
- [3] D. Xiong, X. Li, Z. Bai, S. Lu, Recent advances in layered Ti<sub>3</sub>C<sub>2</sub>T<sub>x</sub> MXene for electrochemical energy storage, *Small* 14 (2018) e1703419.
- [4] D. Xiong, X. Li, Z. Bai, J. Li, H. Shan, L. Fan, C. Long, D. Li, X. Lu, Rational design of hybrid Co<sub>3</sub>O<sub>4</sub>/graphene films: free-standing flexible electrodes for high performance supercapacitors, *Electrochim. Acta* 259 (2018) 338–347.
- [5] N. Blomquist, T. Wells, B. Andres, J. Backstrom, S. Forsberg, H. Olin, Metal-free supercapacitor with aqueous electrolyte and low-cost carbon materials, *Sci. Rep.* 7 (2017) 39836.
- [6] F. Beguin, V. Presser, A. Balducci, E. Frackowiak, Carbons and electrolytes for advanced supercapacitors, *Adv. Mater.* 26 (2014) 2219–2251, 2283.
- [7] Saman Gheyhani, Yanliang Liang, Yan Jing, J.Q. Xu, Y. Yao, Chromate conversion coated aluminium as a lightweight and corrosion-resistant current collector for aqueous lithium-ion batteries, *J. Mater. Chem. A* 4 (2016) 395–399.
- [8] D. Xiong, X. Li, Z. Bai, J. Li, Y. Han, D. Li, Vertically aligned Co<sub>9</sub>S<sub>8</sub> nanotube arrays onto graphene papers as high-performance flexible electrodes for supercapacitors, *Chemistry* 24 (2018) 2339–2343.
- [9] S. Ardizzone, G. Fregonara, S. Trasatti, “Inner” and “outer” active surface of ruo, electrodes, *Electrochim. Acta* 35 (1990) 263–267.
- [10] E. Samuel, H.S. Jo, B. Joshi, H.G. Park, Y.I. Kim, S. An, M.T. Swihart, J.M. Yun, K.H. Kim, S.S. Yoon, High-performance supercapacitors using flexible and freestanding MnO<sub>x</sub>/carbamide carbon nanofibers, *Appl. Surf. Sci.* 423 (2017) 210–218.
- [11] S.D. Perera, M. Rudolph, R.G. Mariano, N. Nijem, J.P. Ferraris, Y.J. Chabal, K.J. Balkus, Manganese oxide nanorod–graphene/vanadium oxide nanowire–graphene binder-free paper electrodes for metal oxide hybrid supercapacitors, *Nano Energy* 2 (2013) 966–975.
- [12] T. Brousse, D. Belanger, J.W. Long, To be or not to be pseudocapacitive? *J. Electrochem. Soc.* 162 (2015) A5185–A5189.
- [13] C. Wu, J. Cai, Q. Zhang, X. Zhou, Y. Zhu, P.K. Shen, K. Zhang, Hierarchical mesoporous zinc-nickel-cobalt ternary oxide nanowire arrays on nickel foam as high-performance electrodes for supercapacitors, *ACS Appl. Mater. Interfaces* 7 (2015) 26512–26521.
- [14] T. Liu, G. Shao, M. Ji, G. Wang, Polyaniline/MnO<sub>2</sub> composite with high performance as supercapacitor electrode via pulse electrodeposition, *Polym. Compos.* 36 (2015) 113–120.
- [15] X.-L. Wu, T. Wen, H.-L. Guo, S. Yang, X. Wang, A.-W. Xu, Biomass-derived sponge-like carbonaceous hydrogels and aerogels for supercapacitors, *ACS Nano* 7 (2013) 3589–3597.
- [16] J. Feng, H. Zhou, J. Wang, T. Bian, J. Shao, A. Yuan, MoS<sub>2</sub> supported on MOF-derived carbon with core-shell structure as efficient electrocatalysts for hydrogen evolution reaction, *Int. J. Hydrogen Energy* 43 (2018) 20538–20545.
- [17] J. Shao, H. Zhou, M. Zhu, J. Feng, A. Yuan, Facile synthesis of metal-organic framework-derived Co<sub>3</sub>O<sub>4</sub> with different morphologies coated graphene foam as integrated anodes for lithium-ion batteries, *J. Alloy. Compd.* 768 (2018) 1049–1057.
- [18] D.K. Lee, K.-S. Choi, Enhancing long-term photostability of BiVO<sub>4</sub> photoanodes for solar water splitting by tuning electrolyte composition, *Nat. Energy* 3 (2017) 53–60.
- [19] N. Campagnol, R. Romero-Vara, W. Deleu, L. Stappers, K. Binnemans, D.E. De Vos, J. Fransaer, A hybrid supercapacitor based on porous carbon and the metal-organic framework MIL-100(Fe), *ChemElectroChem* 1 (2014) 1182–1188.
- [20] D. Ji, H. Zhou, Y. Tong, J. Wang, M. Zhu, T. Chen, A. Yuan, Facile fabrication of MOF-derived octahedral CuO wrapped 3D graphene network as binder-free anode for high performance lithium-ion batteries, *Chem. Eng. J.* 313 (2017) 1623–1632.
- [21] S. Chan, J. Jankovic, D. Susac, M.S. Saha, M. Tam, H. Yang, F. Ko, Electrospun carbon nanofiber catalyst layers for polymer electrolyte membrane fuel cells: structure and performance, *J. Power Sources* 392 (2018) 239–250.
- [22] B.N. Joshi, S. An, Y.I. Kim, E.P. Samuel, K.Y. Song, I.W. Seong, S.S. Al-Deyab, M.T. Swihart, W.Y. Yoon, S.S. Yoon, Flexible freestanding Fe<sub>2</sub>O<sub>3</sub>-SnO<sub>x</sub>-carbon nanofiber composites for Li ion battery anodes, *J. Alloy. Compd.* 700 (2017) 259–266.
- [23] J. Shao, J. Feng, H. Zhou, A. Yuan, Graphene aerogel encapsulated Fe-Co oxide nanocubes derived from Prussian blue analogue as integrated anode with enhanced Li-ion storage properties, *Appl. Surf. Sci.* 471 (2019) 745–752.
- [24] J. Shao, H. Zhou, J. Feng, M. Zhu, A. Yuan, Facile synthesis of MOF-derived hollow

- NiO microspheres integrated with graphene foam for improved lithium-storage properties, *J. Alloy. Compd.* 784 (2019) 869–876.
- [25] B. Joshi, S. Park, E. Samuel, H.S. Jo, S. An, M.-W. Kim, M.T. Swihart, J.M. Yun, K.H. Kim, S.S. Yoon, Zeolitic imidazolate framework-7 textile-derived nanocomposite fibers as freestanding supercapacitor electrodes, *J. Electroanal. Chem.* 810 (2018) 239–247.
- [26] H. Yi, H. Wang, Y. Jing, T. Peng, X. Wang, Asymmetric supercapacitors based on carbon nanotubes@NiO ultrathin nanosheets core-shell composites and MOF-derived porous carbon polyhedrons with super-long cycle life, *J. Power Sources* 285 (2015) 281–290.
- [27] Y. Gao, J. Wu, W. Zhang, Y. Tan, J. Zhao, B. Tang, The electrochemical performance of SnO<sub>2</sub> quantum dots@zeolitic imidazolate frameworks-8 (ZIF-8) composite material for supercapacitors, *Mater. Lett.* 128 (2014) 208–211.
- [28] Xu. Jiao, S. Liu, Y. Liu, Co<sub>3</sub>O<sub>4</sub>/ZnO nanoheterostructure derived from core-shell ZIF-8@ZIF-67 for supercapacitors, *RSC Adv.* 6 (2016) 52137–52142.
- [29] M.S. Javed, H.U. Shah, N. Shaheen, R. Lin, M. Qiu, J. Xie, J. Li, R. Raza, W. Mai, C. Hu, High energy density hybrid supercapacitor based on 3D mesoporous cuboidal Mn<sub>2</sub>O<sub>3</sub> and MOF-derived porous carbon polyhedrons, *Electrochim. Acta* 282 (2018) 1–9.
- [30] L. Wan, E. Shamsaei, C.D. Easton, D. Yu, Y. Liang, X. Chen, Z. Abbasi, A. Akbari, X. Zhang, H. Wang, ZIF-8 derived nitrogen-doped porous carbon/carbon nanotube composite for high-performance supercapacitor, *Carbon* 121 (2017) 330–336.
- [31] B. Han, G. Cheng, E. Zhang, L. Zhang, X. Wang, Three dimensional hierarchically porous ZIF-8 derived carbon/LDH core-shell composite for high performance supercapacitors, *Electrochim. Acta* 263 (2018) 391–399.
- [32] H. Sun, H. Gu, L. Zhang, Y. Chen, Redox deposition of birnessite MnO<sub>2</sub> on ZIF-8 derived porous carbon at room temperature for supercapacitor electrodes, *Mater. Lett.* 216 (2018) 123–126.
- [33] K. Kadota, E. Sivaniah, S. Bureekaew, S. Kitagawa, S. Horike, Synthesis of manganese ZIF-8 from [Mn(BH<sub>4</sub>)<sub>2</sub>.3THF].NaBH<sub>4</sub>, *Inorg. Chem.* 56 (2017) 8744–8747.
- [34] Y. Zhang, F. Liu, End to end assembly of CaO and ZnO nanosheets to propeller-shaped architectures by orientation attachment approaches, *J. Cryst. Growth* 420 (2015) 94–100.
- [35] O.M. Yaghi, H. Furukawa, B. Wang, Preparation of functionalized zeolitic frameworks, Google Patents (2013).
- [36] A.F. Gross, E. Sherman, J.J. Vajo, Aqueous room temperature synthesis of cobalt and zinc sodalite zeolitic imidazolate frameworks, *Dalton Trans.* 41 (2012) 5458–5460.
- [37] P. Xiao, P. Wang, H. Li, Q. Li, Y. Shi, X.L. Wu, H. Lin, J. Chen, X. Wang, New insights into bisphenols removal by nitrogen-rich nanocarbons: synergistic effect between adsorption and oxidative degradation, *J. Hazard. Mater.* 345 (2018) 123–130.
- [38] J. Cravillon, R. Nayuk, S. Springer, A. Feldhoff, K. Huber, M. Wiebecke, Controlling zeolitic imidazolate framework nano- and microcrystal formation: insight into crystal growth by time-resolved in situ static light scattering, *Chem. Mater.* 23 (2011) 2130–2141.
- [39] K. Kida, M. Okita, K. Fujita, S. Tanaka, Y. Miyake, Formation of high crystalline ZIF-8 in an aqueous solution, *CrystEngComm* 15 (2013) 1794–1801.
- [40] G. Zhao, H. Wu, R. Feng, D. Wang, P. Xu, H. Wang, Z. Guo, Q. Chen, Bimetallic zeolitic imidazolate framework as an intrinsic two-photon fluorescence and pH-responsive MR imaging agent, *ACS Omega* 3 (2018) 9790–9797.
- [41] J.B. Bharate, S.K. Guru, S.K. Jain, S. Meena, P.P. Singh, S. Bhushan, B. Singh, S.B. Bharate, R.A. Vishwakarma, Cu–Mn spinel oxide catalyzed synthesis of imidazo [1,2-a]pyridines through domino three-component coupling and 5-exo-dig cyclization in water, *RSC Adv.* 3 (2013) 20869.
- [42] Q.-H. Wu, M. Liu, W. Jaegermann, X-ray photoelectron spectroscopy of La<sub>0.5</sub>Sr<sub>0.5</sub>MnO<sub>3</sub>, *Mater. Lett.* 59 (2005) 1980–1983.
- [43] C. Cai, Y. Zou, C. Xiang, H. Chu, S. Qiu, Q. Sui, F. Xu, L. Sun, A. Shah, Broccoli-like porous carbon nitride from ZIF-8 and melamine for high performance supercapacitors, *Appl. Surf. Sci.* 440 (2018) 47–54.
- [44] M. Shatnawi, A.M. Alsmadi, I. Bsoul, B. Salameh, M. Mathai, G. Alnawashi, G.M. Alzoubi, F. Al-Dweri, M.S. Bawa'aneh, Influence of Mn doping on the magnetic and optical properties of ZnO nanocrystalline particles, *Results Phys.* 6 (2016) 1064–1071.
- [45] T. Purkait, G. Singh, D. Kumar, M. Singh, R.S. Dey, High-performance flexible supercapacitors based on electrochemically tailored three-dimensional reduced graphene oxide networks, *Sci. Rep.* 8 (2018) 640.
- [46] M.D. Stoller, R.S. Ruoff, Best practice methods for determining an electrode material's performance for ultracapacitors, *Energy Environ. Sci.* 3 (2010) 1294–1301.
- [47] M. Jiang, X. Cao, D. Zhu, Y. Duan, J. Zhang, Hierarchically porous N-doped carbon derived from ZIF-8 nanocomposites for electrochemical applications, *Electrochim. Acta* 196 (2016) 699–707.
- [48] X. Li, C. Hao, B. Tang, Y. Wang, M. Liu, Y. Wang, Y. Zhu, C. Lu, Z. Tang, Supercapacitor electrode materials with hierarchically structured pores from carbonization of MWCNTs and ZIF-8 composites, *Nanoscale* 9 (2017) 2178–2187.
- [49] B. Lin, Yidong Zhang, Junchuan Wang, Jiahui Tian, Ying Sun, Xueqin Zhang, Hong Yang, All-solid-state asymmetric supercapacitors based on ZnO quantum dots/carbon/CNT and porous Ndoped carbon/CNT electrodes derived from a single ZIF-8/CNT template, *J. Mater. Chem. A* 4 (2016) 10282.
- [50] W. Bao, A.K. Mondal, J. Xu, C. Wang, D. Su, G. Wang, 3D hybrid-porous carbon derived from carbonization of metal organic frameworks for high performance supercapacitors, *J. Power Sources* 325 (2016) 286–291.
- [51] Rahul R. Salunkhe, Yuichiro Kamachi, Nagy L. Torad, Soo Min Hwang, Ziqi Sun, Shi Xue Dou, J.H. Kim, Y. Yamauchi, Fabrication of symmetric supercapacitors based on MOF-derived nanoporous carbons, *J. Mater. Chem. A* 2 (2014) 19848–19854.
- [52] Christine Young, Rahul R. Salunkh, Jing Tang, Hu Chi-Chang, Mohammed Shahabuddin, Ekrem Yanmaz, Md. Shahriar A. Hossain, Jung Ho Kimb, Y. Yamauchi, Zeolitic imidazolate framework (ZIF-8) derived nanoporous carbon: the effect of carbonization temperature on the supercapacitor performance in an aqueous electrolyte, *PCCP* 18 (2016) 29308.
- [53] Y. Wang, B. Chen, Y. Zhang, L. Fu, Y. Zhu, L. Zhang, Y. Wu, ZIF-8@MWCNT-derived carbon composite as electrode of high performance for supercapacitor, *Electrochim. Acta* 213 (2016) 260–269.
- [54] L. Xin, Q. Liu, J. Liu, R. Chen, R. Li, Z. Li, J. Wang, Hierarchical metal-organic framework derived nitrogen-doped porous carbon/graphene composite for high performance supercapacitors, *Electrochim. Acta* 248 (2017) 215–224.
- [55] L. Kong, Q. Chen, X. Shen, Z. Xu, C. Xu, Z. Ji, J. Zhu, MOF derived nitrogen-doped carbon polyhedrons decorated on graphitic carbon nitride sheets with enhanced electrochemical capacitive energy storage performance, *Electrochim. Acta* 265 (2018) 651–661.
- [56] L. Xin, R. Li, Z. Lu, Q. Liu, R. Chen, J. Li, J. Liu, J. Wang, Hierarchical metal-organic framework derived nitrogen-doped porous carbon by controllable synthesis for high performance supercapacitors, *J. Electroanal. Chem.* 813 (2018) 200–207.